metals

MDPI

Article

The Effect of Heat Accumulation on the Local Grain Structure in Laser-Directed Energy Deposition of Aluminium

Christian Hagenlocher [1,*], Patrick O'Toole [1], Wei Xu [2], Milan Brandt [1], Mark Easton [1] and Andrey Molotnikov [1]

[1] Centre for Additive Manufacturing, School of Engineering, RMIT University, Melbourne, VIC 3000, Australia
[2] School of Engineering, Deakin University, Geelong, VIC 3216, Australia
* Correspondence: christian.hagenlocher@ifsw.uni-stuttgart.de

Abstract: The energy used to melt the material at each layer during laser-directed energy deposition (L-DED) accumulates in the solidified layers upon layer deposition and leads to an increase in the temperature of the part with an increasing number of layers. This heat accumulation can lead to inhomogeneous solidification conditions, increasing residual stresses and potentially anisotropic mechanical properties due to columnar grain structures. In this work, infrared imaging is applied during the directed energy deposition process to capture the evolution of the temperature field in high spatial and temporal evolutions. Image processing algorithms determined the solidification rate and the temperature gradient in the spatial and temporal evolutions and evidenced their change with the proceeding deposition process. Metallographic analysis proves that these changes significantly affect the local grain structure of the L-DED fabricated parts. The study provides comprehensive quantitative measurements of the change in the solidification variables in local and temporal resolutions. The comprehensive comparison of different parameter combinations reveals that applied power, and especially the frequency of the consecutive deposition of the individual layers, are the key parameters to adjusting heat accumulation. These findings provide a methodology for optimising L-DED manufacturing processes and tailoring the local microstructure development by controlling heat accumulation.

Keywords: directed energy deposition; solidification; grain structure; temperature evolution; heat accumulation

Citation: Hagenlocher, C.; O'Toole, P.; Xu, W.; Brandt, M.; Easton, M.; Molotnikov, A. The Effect of Heat Accumulation on the Local Grain Structure in Laser-Directed Energy Deposition of Aluminium. *Metals* **2022**, *12*, 1601. https://doi.org/10.3390/met12101601

Academic Editor: Maurizio Vedani

Received: 29 August 2022
Accepted: 20 September 2022
Published: 25 September 2022

1. Introduction

In additive manufacturing (AM), three-dimensional parts are produced in a layer-by-layer fashion. These parts can incorporate additional functionality and a reduction in material waste compared to the conventional subtractive manufacturing processes and casting. Notably, laser-directed energy deposition (L-DED) is suitable for manufacturing complex components on a large scale for several industries, such as the space and energy sectors.

The microstructure has a significant influence on the strength and ductility of such components [1–4], which results from the local solidification conditions of the individual beads and layers. A large number of L-DED studies report the formation of columnar grains [5–7], which is affected by the height of a component [5,8,9]. These components typically possess anisotropic mechanical properties, which limit their application in industrial settings [4–6,10,11]. The manufacturing of components also requires many trials to determine suitable processing parameters, such as laser power, velocity, layer thickness, gas flow and strategies, such as layer geometry, pattern, and frequency.

The absolute value of the local temperature gradient G and the solidification rate R, i.e., the velocity of the local solidification, define the local grain structure of each layer after solidification [12]. Figure 1 shows a schematic of the solidification during a DED of a bead

on a previous layer in a thin wall structure, which already consists of multiple superimposed layers of deposited beads. The added material solidifies between the isotherms of its liquidus temperature, T_{Liquid}, and its solidus temperature, T_{Solid}, which are represented, respectively, by the black dashed line and the blue line. The local temperature gradient $G(x,z)$ (purple arrow) describes the local change in the temperature field.

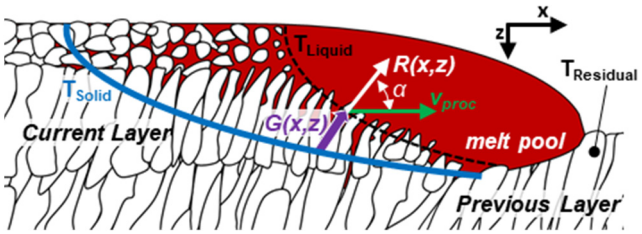

Figure 1. Sketch of the local solidification processes in a subsequent layer, which is added onto a previous layer in L-DED manufacturing (adapted from [13]). The laser beam moves from left to right in a positive x- direction. Red areas represent liquid, and white areas are solid materials. The liquidus isotherm (dashed black line) and solidus isotherm (blue line) confine the solidification zone.

The grains grow in the direction of the local temperature gradient $G(x,z)$, which is perpendicular to the liquidus isotherm, T_{Liquid}. The solidification rate (white arrow)

$$R(x,z) = v_{proc} \cdot \cos\alpha(x,y)\Big|_{(x,y)_{T_{Liquid}}} \quad (1)$$

in a quasi-stationary temperature field is directly connected with the velocity of the movement of the laser beam, v_{proc}, and the cosine of the local angle $\alpha(x,z)$ between the vector of the solidification rate (white arrow) and the vector of the process velocity, v_{proc} (green arrow) [12]. Presuming a quasi-stationary temperature field, the multiplication of G with R yields the local cooling rate

$$\dot{T}(x,z) = \frac{dT}{dt} = G(x,z) \cdot R(x,z). \quad (2)$$

An increased cooling rate, $\dot{T}$, promotes nucleation [14,15], i.e., the refinement of the grain size [12,16,17]. The G/R ratio represents a simplified criterion for the solidification mode [12]. An oriented columnar growth of grains appears in the case of high G/R values, while low G/R leads to the growth of equiaxed dendritic grains [12,16]. Such a refined equiaxed grain structure is favourable, as it leads to enhanced and isotropic mechanical behaviour [3,4,18,19].

Therefore, many studies focus on obtaining a homogeneous microstructure with fine equiaxed grains. The main strategy pursued by the majority of studies is to modify the alloy composition [9,18,20,21] and introduce grain refiners, which can promote nucleation [18,19,21–23].

It is well known from welding that the applied laser power and the process velocity have a strong influence on the temperature field [24–26], which defines the temperature gradient and the shape of the isotherms, i.e., the solidification rate. Previous studies demonstrated that local solidification could be positively influenced by optimising the processing parameters, leading to the desired equiaxed grain structure of laser beam welds [26,27]. The results of Froend et al. and Wang et al. [4,28–30] indicate that the same approach can be adopted in additive manufacturing processes if the influence of the process parameters on the local grain structure is known.

The subsequent addition of the individual layers leads to a cumulative heat input during additive manufacturing, which results in a continuous increase in the residual temperature, $T_{Residual}$, of the previously added layer [29,31–33]. The L-DED of powder or wire enables the addition of material at high volume rates [7]. This results in a high layer-

specific heat input at a high frequency, which leads to heat accumulation during the build. The accumulated heat in the previously deposited layers affects the temperature field [29] and the local solidification in addition to the conventional process parameters [34], e.g., laser power and process velocity. This results in local changes in the grain structure with its size and morphology, which in turn affect the local mechanical characteristics [4,6,8,9,11,30].

In order to capture this effect experimentally, here, the change in the temperature field was recorded by an infrared camera during the L-DED manufacturing of aluminium parts, as previously described in [13]. The experiments aim to capture, for the first time, a comprehensive quantitative measurement of all relevant solidification variables in L-DED processes in local and temporal resolutions, including its comparison to the resulting microstructure. The local temperature gradient, solidification rate, and cooling rate were deduced from the IR images by the image processing algorithms presented in [13] and compared with metallographic analysis. The captured data are useful values for the validation and calibration of thermal/solidification modelling. Furthermore, such experimental data provide fundamental knowledge about the solidification in the L-DED process required for the development of L-DED-specific materials. Finally, the influence of different process parameters is evaluated, and the implications of the new findings on process design are discussed.

2. Experimental

Rectangular columns were manufactured by L-DED using AlMg5 alloy wire, and the setup was presented in previous work [13,35], as shown in Figure 2.

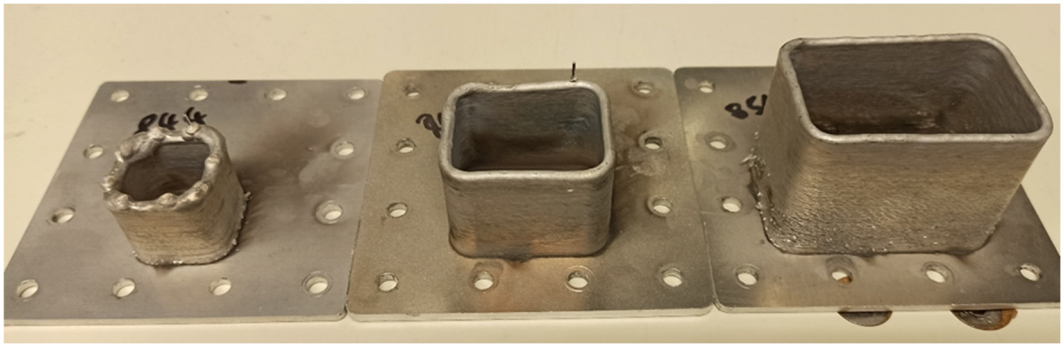

Figure 2. Picture of the sample geometries built at a laser power of 4200 W and a process velocity of 4.5 m/min with different perimeters of 107.12 mm (**left**), 167.12 mm (**middle**), and 217.12 mm (**right**).

The schematic of the L-DED process and equipment is shown in Figure 3a. The AlMg5 wire, with a diameter of 1 mm, was fed coaxially to the laser beam using a CoaxPrinter® head from Precitec. The axicon objective of the CoaxPrinter® generates an annular intensity distribution with a diameter of about 2.8 mm at a working distance of 104 mm, which surrounds the wire in its centre.

The monitoring of the deposition process is performed using the infrared camera VarioCam HD head900 from InfraTec. The camera is fixed stationary to the L-DED-manufactured sample, which ensures a focused image during the whole processing time. The plane surface of the observed sidewall ensures that the image is in the focal plane of the infrared camera, where the optical axis is oriented normal to the observed surface. Thus, the recorded images capture the two-dimensional temperature distribution of the entire sidewall, which is built at a particular point in time. Metallographic analysis in [4,5] demonstrate the presence of this two-dimensional temperature distribution over the total wall thickness in the case of L-DED manufacturing of thin aluminium walls. The cross-sections constantly show an almost horizontal orientation of the characteristic microstructures, which identify the individual layers [4,5]. Additionally, the closed contour enables a continuous process without changes in the process direction or interruptions for repositioning the process head.

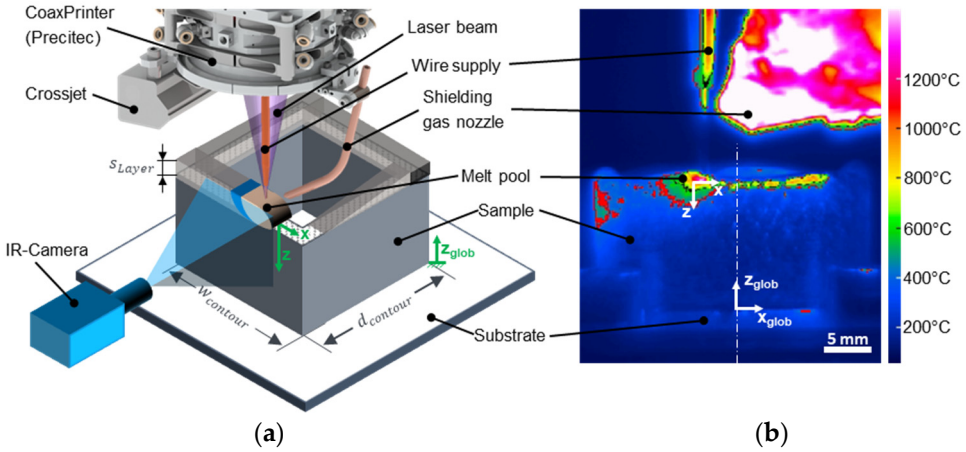

Figure 3. Sketch of the experimental setup (**a**) and an infrared image of the process (**b**). Infrared videos can be found in the Supplementary data.

The IR-Camera VarioCam HD head900 records images with a size of 1024 × 768 pixels in a spectral range of 7.5–14 µm with a frame rate of 30 Hz, which results in a maximum exposure time of t_{shut} = 33.33 ms. The telescope's objective results in a scale of 9.6 px/mm. According to the calibration experiment presented in previous work [13], the emissivity of the DED-manufactured surface was determined to be ε = 0.07, which is in the range of the literature values for different aluminium surface conditions [36–38].

Figure 3b shows an exemplary image, which was recorded with the infrared camera during DED manufacturing. The colour scale represents the local temperature determined by the local emission of thermal radiation at an emissivity of ε = 0.07. The Supplementary data of this work contains three exemplary infrared videos, and the raw data of all recorded temperature fields are available at [39].

The samples were built on an AlMg3 substrate sheet with a thickness of 3 mm, which was fixed with 12 bolts on a water-cooled aluminium substrate to ensure constant heat extraction. The rectangular parts with the width, $w_{contour,}$ and depth, $d_{contour,}$ were built without dwell times or other interruptions by continuously adding the individual layers. The thickness of the applied layers, s_{Layer}, was predefined by a constant gradual increase in the z_{glob}-position of the CoaxPrinter® processing head by 0.5 mm per layer. To reduce the local acceleration maxima, the corners of all rectangular columns were smoothed using a radius of $r_{contour}$ = 7.5 mm.

This work defines two different coordinate systems, as represented by the white arrows in Figure 3b. The stationary x_{glob}-z_{glob}-system origin is set at the substrate surface and the centreline of the observed sidewall of the DED-manufactured part, and the x-z-systems follow the position of the melt pool during the DED process, as described in our previous work [13]. Figure 4 presents a typical IR image of the processing zone. The image processing algorithm, which is presented in our previous work [13], allows for an extraction of the geometry of the isotherms of the solidification zone in the x-z coordinate system. The origin of x is located at the maximum extension z_{max} of the liquidus isotherm in the z-direction, and the origin of the z-axis is defined to be located at the position of the maximum extension x_{max} of the liquidus isotherm in the negative x-direction, as depicted inFigure 4. This definition ensures that the melting processes are located at $x > 0$ and solely solidification takes place at $x < 0$ and $z > 0$. The determined isotherms are shown below in Figure 4 with solid lines for $T_{Liquidus}$ and dashed lines for $T_{Solidus}$ during the deposition of the10th layer (blue), 30th layer (green), and 50th layer (red). Note that there is no direct connection between this definition of the coordinates' origin and the position of the laser beam, as the definition of the origin of the coordinates individually depends on the shape of each isotherm in each layer.

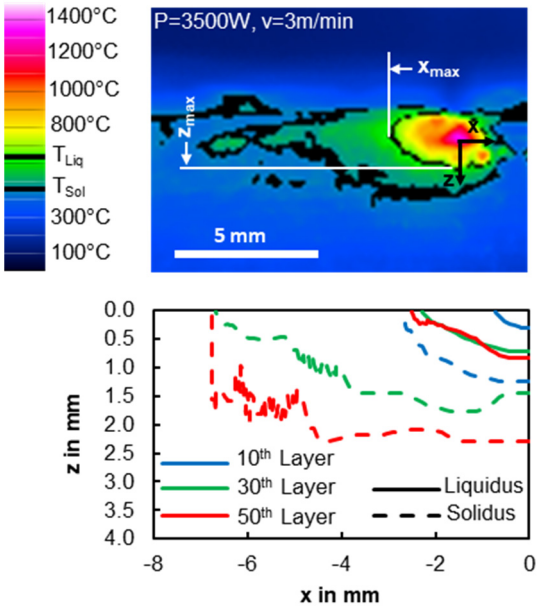

Figure 4. Temperature distribution after 30 layers and liquidus and solidus isotherms after 10, 30, and 50 layers (Note: The origin of the coordinate system depends on the respective maxima of the corresponding isotherms).

To identify the influence of the process parameters, three different process velocities (v_{proc}) were investigated. As listed in Table 1, the laser power, P, and the wire feed rate, v_{wire}, were adapted to the process velocity, v_{proc}. The influence of the heat accumulation on the resulting microstructure was studied by varying the frequency of layer application, which is defined as:

$$f_{Layer} = \frac{v_{proc}}{l_{contour}}, \tag{3}$$

where $l_{contour} = 2w_{contour} + 2d_{contour} + 2\pi r_{contour}$.

Table 1. Investigated parameter combinations.

Process Velocity v_{proc} in m/min	Laser Power P in W	Wire Feed Rate v_{wire} in m/min	Contour Width $w_{contour}$ in mm	Contour Depth $d_{contour}$ in mm	Total Perimeter $l_{contour}$ in mm	Layer Frequency f_{Layer} in Hz
1.5	2400	2.5				0.233
3	3500	5	30	30	107.124	0.467
4.5	4200	7.5				0.700
1.5	2400	2.5				0.15
3	3500	5	50	40	167.124	0.299
4.5	4200	7.5				0.449
3	3500	5	70	45	217.124	0.230
4.5	4200	7.5				0.345

The shielding gas nozzle covered the processing zone with a flow rate of 35 L/min to prevent excessive oxidation during the DED process.

3. Results

For the sake of clarity, the analysis presented in the following covers the samples with a perimeter of about 107 mm. The results, determined in the case of the larger perimeters, are presented in Appendix A.

3.1. Temporal Evolution of the Residual Temperature

The black curves in Figure 5 represent the average measured temperature of the current layer at $z = 0$ at the centreline of the observed side wall at $x_{glob} = 0$ when manufacturing the parts with a perimeter of $l_{contour} \approx 107$ mm. The temperature value represents the average within an area, with the height of the current layer between $0 < z < 0.5$ mm and a width of $-v_{proc} \cdot t_{shut} < x_{glob} < v_{proc} \cdot t_{shut}$ of three analysed samples as a function of time (lower horizontal axis) and a number of layers (upper horizontal axis). The grey scatter band represents the deviation of the minimum and maximum measured values within the whole range $-v_{proc} \cdot t_{shut} < x_{glob} < v_{proc} \cdot t_{shut}$ and $0 < z < 0.5$mm of three analysed DED processes with the respective process parameters.

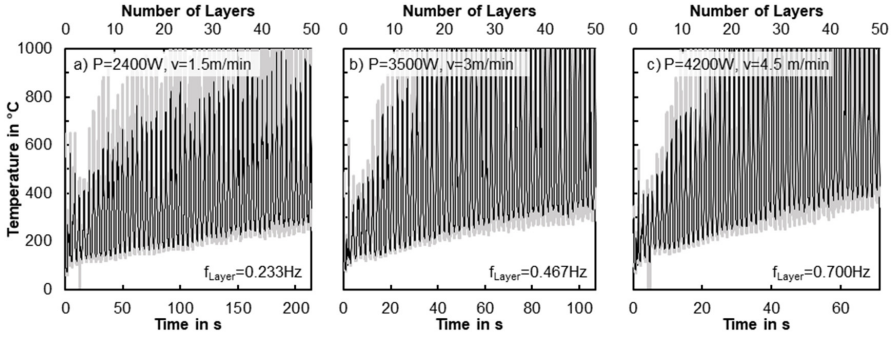

Figure 5. Average temperature at $z = 0^{+0.5}_{-0}$ and $x_{glob} = 0 \pm v_{proc} \cdot t_{shut}$ as a function of time during L-DED manufacturing of rectangular parts with a perimeter of $l_{contour} \approx 107$ mm at a laser power of 2.4 kW and a process velocity of 1.5 m/min (**a**), 3.5 kW and 3 m/min (**b**), and 4.2 kW and 4.5 m/min (**c**). The grey scatter band represents the minimum and maximum deviation of all pixels within $z = 0^{+0.5}_{-0}$ and $x_{glob} = 0 \pm v_{proc} \cdot t_{shut}$ within three repetitive measurements.

The periodic character of the curve shows the layer-wise heat input during the deposition. The peaks of the local maxima result from the presence of the laser beam within the analysed area at $0 < z < 0.5$ mm and—$v_{proc} \cdot t_{shut} < x_{glob} < v_{proc} \cdot t_{shut}$. After each maximum, the temperature decreases until the laser beam passes again while adding the next layer. The local minima represent the residual temperature, $T_{Residual}$, of the previous layer before the next layer is added. The accumulation of the heat, which is introduced with each layer, leads to a continuous increase in this residual temperature within the 50 layers. The comparison of the curves in Figure 5 shows that the higher velocity of 4.5 m/min, i.e., higher layer frequency, and higher laser power of 4200 W (Figure 5c) lead to a significantly higher residual temperature than the lower velocities and laser powers, which are demonstrated by the monotonic increase in the minimum temperature of the curves in Figure 5a,b.

3.2. Temporal Evolution of Solidification Conditions

The effect of the change in the temperature distribution with an increasing build height, i.e., the number of layers, on the solidification conditions is analysed by the determination of the temperature gradient, solidification rate, the consequent cooling rate, and G/R ratio at the two representative positions of the liquidus isotherms, where $x = 0$ and $z = 0$. These positions represent the expected location of the extrema of the local temperature gradient during solidification in a temperature field of a moving heat source [12,24]. The minimum local temperature gradient, G_x, during solidification in such a temperature distribution follows the direction of the heat source movement, i.e., in the x-direction, and is located at the maximum extension of the liquidus isotherm in the x-direction, where $z = 0$ in the defined x-z-coordinates [12,24]. The maximum temperature gradient, G_z, during solidification in the temperature distribution of a moving heat source follows the z-direction exclusively at the position of the maximum extension of the liquidus isotherm, where $x = 0$ in the defined x-z-coordinates [12,24].

Figure 6 compares the influence of the increasing build height on the maximum and minimum temperature gradients during solidification. The results of three different process parameter combinations can be distinguished by the different colours. The data points for G_x in Figure 6a and G_z in Figure 6b represent the average of all the determined gradients of the respective position and direction between $T_{Liquidus}$ and $T_{Solidus}$ for three repeat measurements. The length of the error bars represents the range between the minimum and maximum determined values of all temperature gradients within this captured data set of the respective parameter combination.

The large error bars for the first 15 layers imply that the determined values within this range are not reliable. These large variations result from reflections of the laser beam and the thermal radiation on the substrate surface, which is close to the processing zone at low build heights. Above 15 layers, the determined temperature gradients show a more reasonable scatter. After the first 15 layers, a significant decrease in the G_x and G_z gradients is observed, except in the case of G_z, at the lowest velocity of 1.5 m/min, where the increase in the residual temperature is also least pronounced, as shown in Figure 5a. These results demonstrate that the decrease in the temperature gradient is associated with the increased residual temperature and is a consequence of heat accumulation.

The comparison of the absolute values of G_x (Figure 6a) and G_z (Figure 6b) above 15 layers shows that higher temperature gradients are found in the case of G_z. The higher velocity and laser power, and thus the highest heat accumulation (green data points), result in the lowest temperature gradients in the x-direction (Figure 6a), while these parameters lead to the maximum temperature gradients in the z-direction (Figure 6b). In the case of L-DED manufacturing with a lower velocity and laser power (red data points), this relationship is reversed: the maximum temperature gradients in the x-direction result from the lowest process velocity, as shown in Figure 6a, while the respective temperature gradient in the z-direction shows lower values in Figure 6b.

The increase in the residual temperature (Figure 5), and the decrease in the temperature gradients (Figure 6), change the shape of the isotherms, as seen in Figure 4. According to Equation (1), this inevitably leads to a change in the local solidification rate. It should be noted that the local solidification rate in the x-direction at $z = 0$ is largely independent of the heat accumulation, since it is predefined by the value of the process velocity in the case of a quasi-stationary temperature field [12]. This can be reasonably assumed within the time frame of the deposition of one layer. The constant value of the solidification rate at $z = 0$, which is only defined by the process velocity, is shown in Figure 7a. The increase in the z-position that follows the shape of the liquidus isotherm is accompanied by a decrease in the local solidification rate, which is reflected by the cosine of the angle, α, defined in Equation (1). Based on this definition, the maximum possible solidification rate is limited to the value of the process velocity, which is present at $z = 0$ where $\alpha = 0°$. However, a new layer remelts the upper region of its preceding layer, which solidified at $z = 0$ with the maximum solidification rate. Hence, the remaining grain structure of an L-DED-manufactured part is determined by the lower solidification rates, which are present in the lower region of the melt pool. In order to access a representative quantitative value for the solidification rate in the lower region of the melt pool, the average of all the local solidification rates within the lowest 0.5 mm of the melt pool was determined. For this, the local solidification rates were determined by Equation (1) within the range of $(z_{max}\text{-}0.5) < z < z_{max}$ from the local angles $\alpha(z)$ of the extracted liquidus isotherms, as shown in Figure 4. The data points in Figure 7b represent the average of all the determined values within the range of $(z_{max}\text{-}0.5) < z < z_{max}$ while depositing a layer at the respective build height. The length of the error bars represents the range between the minimum and maximum determined values within the range of $(z_{max}\text{-}0.5) < z < z_{max}$ in three repetitive measurements.

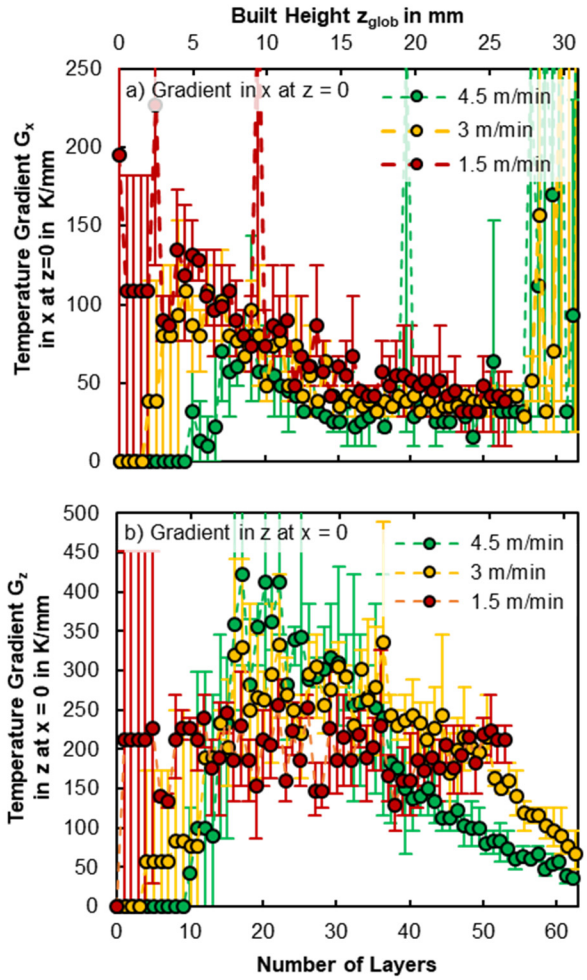

Figure 6. Average temperature gradients during solidification at z = 0 (**a**) and x = 0 (**b**) as a function of the number of added layers and build height in the case of DED manufacturing of parts with a perimeter of $l_{contour} \approx 107$ mm for different process parameter combinations.

The reflection on the substrate surface, as mentioned above, also leads to some uncertainty for the average solidification rates during the first 15 layers, which is also reflected in the large error bars in Figure 7b. Above 15 layers, the average solidification rate of the lower part of the melt pool strongly depends on the process velocity. DED manufacturing with 4.5 m/min, as shown with the green data points in Figure 7b, results in significantly higher values of average solidification rates than in the case of DED manufacturing with 1.5 m/min, as shown with the red data points in Figure 7b. The average values in Figure 7b show a slight decrease in the solidification rate with increasing build height. However, compared to the decrease in the temperature gradient in Figure 6, the decrease in the solidification rate is less pronounced in the case of all the analysed parameter combinations. This further implies that the major effect that heat accumulation has on solidification is ascribed to a change in the temperature gradient.

As described in the introduction, the G/R ratio determines the morphology of the grain structure, while the cooling rate ($G{\cdot}R$) is related to the size of the grains. The determined temperature gradients and solidification rates are used to determine the G/R ratio in Figure 8a,b and the cooling rate in Figure 8c,d. The length of the error bars represents the range between the minimum and maximum values resulting from the minimum and maximum deviations of the temperature gradient and solidification rate. Note that the maximum deviation of the G/R ratio results from the maximum temperature gradient and the minimum solidification rate and vice versa for the minimum deviation of the G/R ratio.

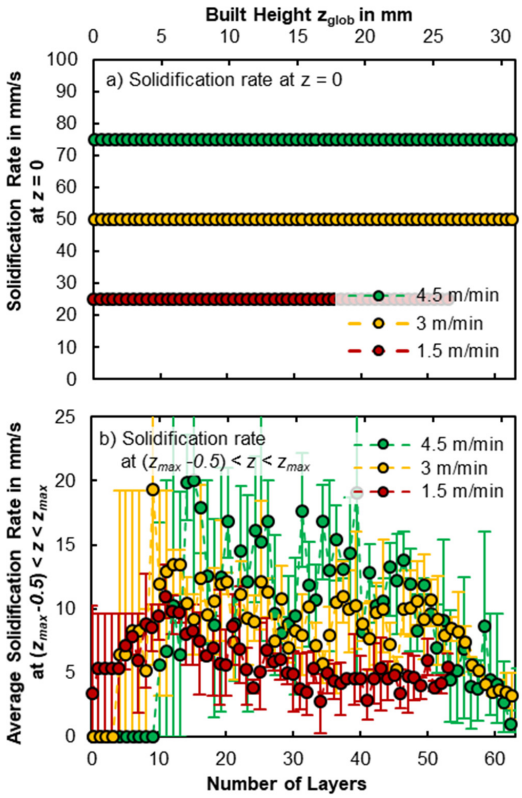

Figure 7. Average solidification rate at z = 0 (**a**) and x = 0 (**b**) as a function of the number of added layers and build height z_{glob} in the case of DED manufacturing of parts with a perimeter of $l_{contour} \approx 107$ mm for different process parameter combinations.

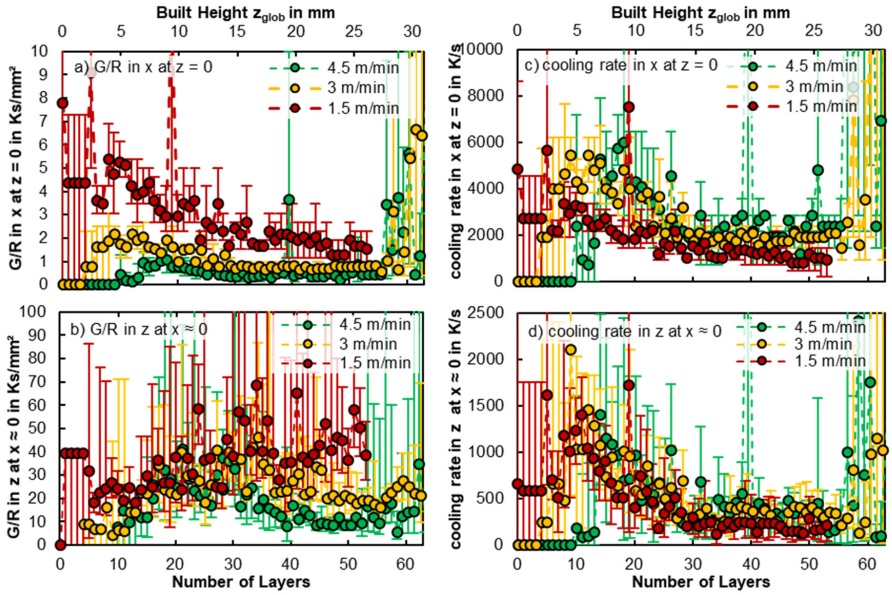

Figure 8. G/R ratio at $z = 0$ (**a**) and $x = 0$ (**b**) and cooling rate $z = 0$ (**c**) and $x = 0$ (**d**) as a function of the number of added layers and build height z_{glob} in the case of L-DED manufacturing of parts with a perimeter of $l_{contour} \approx 107$ mm for different process parameter combinations.

The significant decrease in the temperature gradient with an increasing build height, in the case of all the parameter combinations, leads to a substantial decrease in the G/R ratio at $z = 0$ (Figure 8a) and a decrease in the cooling rate at $z = 0$ and $x \approx 0$, (Figure 8c,d). The maximum cooling rates in the x- and z-directions are achieved at the highest considered

velocity of 4.5 m/min. The decrease in the cooling rate converges to an approximately constant value after about 30 layers.

The G/R ratio in the x-direction at $z = 0$ shows the most pronounced decrease in the case of L-DED manufacturing at the lowest velocity of 1.5 m/min. This is a result of the larger decrease in its respective temperature gradient, as shown in Figure 6a.

The parameter combination with the highest velocity of 4.5 m/min is the only one that shows a significant decrease in the G/R ratio at $x \approx 0$ with increasing build height z_{glob} (Figure 8b). The lowest process velocity of 1.5 m/min and laser power of 2400 W (red data points in Figure 8b) even shows an increase in the G/R ratio. This can be explained by the marginally pronounced decrease in the temperature gradient shown in Figure 6b in combination with the excessive scatter of the solidification rate shown in Figure 7b.

These results show that the major influence of the decreasing temperature gradient on the solidification conditions is a consequence of the increasing residual temperature resulting from the layer-by-layer heat accumulation during DED manufacturing.

3.3. Change in Grain Structure

Figure 9 presents the metallographic sections of the samples with a perimeter of $l_{contour} \approx 107$ mm, from the processes analysed in Sections 3.1 and 3.2. The DED-manufactured samples were mechanically ground, polished, and anodically etched using Barker's reagent [40]. The subsequent illumination with polarised light yields an appearance of the individual grains in different colours according to their grain orientation. In the following, we refer to the grains as columnar grains if their length exceeds their width by at least twice and which grow over the entire layer height. Grains whose length is less than twice their width are referred to as equiaxed grains.

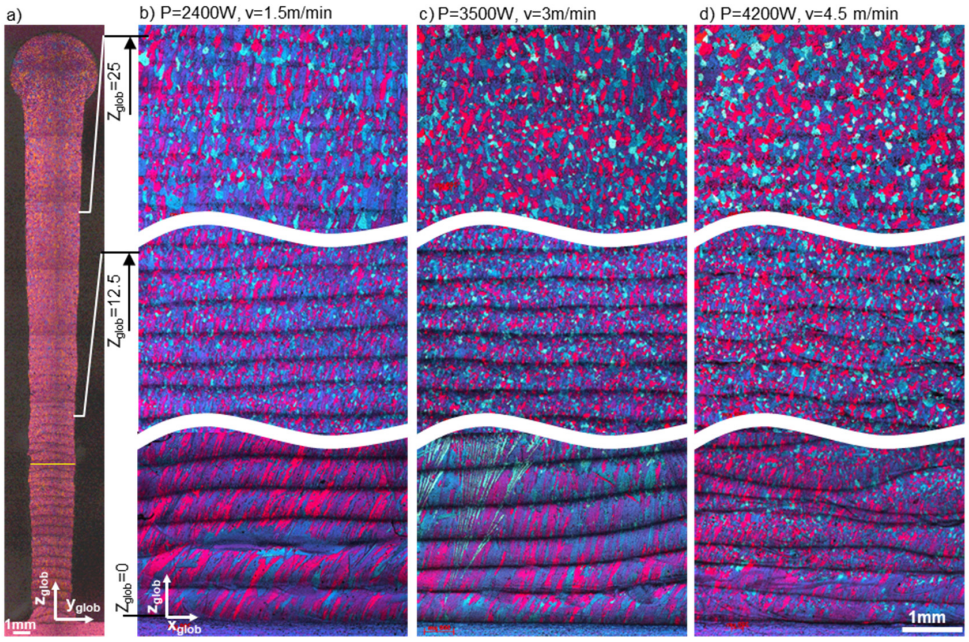

Figure 9. Cross-section in the y_{glob}-z_{glob}-plane of the entire wall of a sample with a perimeter of $l_{contour} \approx 107$ mm, built with a process velocity of 4.5 m/min and a laser power of 4200 W, (**a**) and local longitudinal sections in the x_{glob}-z_{glob}-plane at different build heights z_{glob} of samples with a perimeter of $l_{contour} \approx 107$ mm, built with a process velocity of 1.5 m/min and a laser power of 2400 W (**b**), a process velocity of 3 m/min and a laser power of 3500 W (**c**), a process velocity of 4.5 m/min and a laser power of 4200 W (**d**). All analysed cross-sections are available at [39].

The cross-section in Figure 9a represents the y_{glob}-z_{glob}-plane of the whole wall of a sample, which was built with a process velocity of 4.5 m/min and a laser power of 4200 W. The resulting cross-sections of all the parameter combinations listed in Table 1 are available

in [39]. The longitudinal sections in Figure 9b–d represent the metallographically prepared surfaces in the y_{glob}-z_{glob}-plane of the different parameter combinations listed in Table 1 in the range of the build heights $0 < z_{glob} < 2.5$ mm (bottom row), $10 < z_{glob} < 12.5$ mm (middle row) and $22.5 < z_{glob} < 25$ mm (top row).

The geometry of the cross-section in Figure 9a shows an increasing wall thickness with an increasing build height z_{glob}. This is an additional consequence of the heat accumulation, which leads to an increasing melt pool size as a result of the increasing residual temperature, $T_{Residual}$, as shown in Figures 4 and 5. Above $z_{glob} = 35$ mm, heat accumulation raises the residual temperature above the liquidus temperature at z = 0 for the process velocity of 4.5 m/min and laser power of 4200 W. In this case, the newly added material within the current layer remains in the liquid state. This behaviour limits the possible maximum build height and results in the circular accumulation of material at the top of the wall in Figure 9a or other disturbances of the upper layers, as shown in Figure 1.

The variation in the G/R ratio, shown in Figure 8, results in an obvious change in the local morphology of the grain structure along the build height z_{glob}. Especially in the case of DED manufacturing with lower velocities, such as 1.5 m/min and 3 m/min, the morphology in the lower region of the samples is primarily dominated by the oriented columnar grains, as shown in the bottom row of Figure 9b,c. For the highest velocity of 4.5 m/min, equiaxed dendritic grains start to appear in the first five layers along the longitudinal section, as shown in the bottom row of Figure 9d. This is a consequence of the low absolute values of the G/R ratios, as shown in Figure 8.

In the region of $10 < z_{glob} < 12.5$ mm, the grain structure changes to a fully equiaxed morphology for the process velocities of 3 m/min and 4.5 m/min (middle row of Figure 9c,d), while it still shows an oriented columnar character in the case of a velocity of 1.5 m/min (middle row of Figure 9b). A similar grain structure is observed in the region of $22.5 < z_{glob} < 25$ mm, where the longitudinal section in the case of DED manufacturing with a velocity of 1.5 m/min still shows an oriented character of a columnar morphology in the top row of Figure 9b. Additionally, one can observe a coarsening of the grain structure in the region of $22.5 < z_{glob} < 25$ mm compared to $10 < z_{glob} < 12.5$ mm for all parameter combinations present in Figure 9.

In order to quantify those changes in morphology and size of the local grain structures, the cross-sections of every fifth layer were analysed in detail. For the purpose of local morphology quantification in the respective layer, three horizontal reference lines at three positions within the respective layer were drawn. An example is shown by the yellow line in Figure 9a; the total length of the reference lines corresponds to the local wall width. Subsequently, the length of the share of the reference line, which cuts oriented columnar grains, was measured. The ratio between the length, which cuts oriented columnar grains, and the total length of the reference line yields the proportion of the oriented columnar grains at the analysed vertical position. The data points in Figure 10a represent the average value of three analysed horizontal lines within each analysed layer in each of the three built samples. The size of the error bars represents the range between the minimum and the maximum of these nine determined values for each analysed layer at the corresponding height z_{glob}.

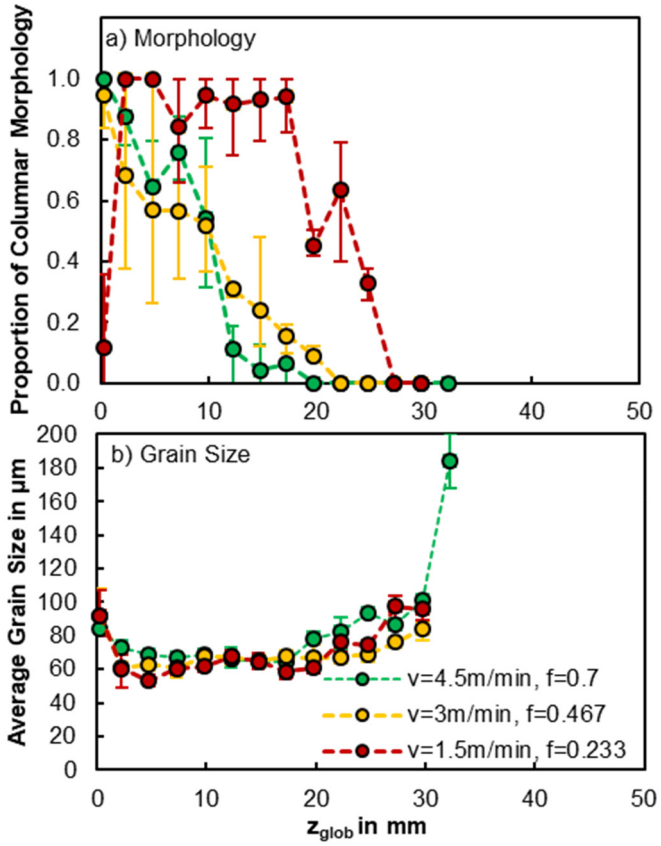

Figure 10. Proportion of morphology (**a**) and size (**b**) of the grain structure determined from the cross-sections of the DED-manufactured samples. Micrographs of all cross-sections are available at [39].

In order to quantify the average grain size, the number of grains—which were cut by the horizontal reference lines—was determined according to DIN EN ISO 643 [41]. The division of the length of the reference lines, i.e., the local wall thickness, by the determined number of grains yields the average local grain size according to DIN EN ISO 643 [41]. This average grain size describes the average diameter for an equiaxed morphology and the average width for columnar grains, whose orientation is almost perpendicular to the reference line, as shown in the longitudinal sections of Figure 9. The data points in Figure 10b represent the average value of all determined grain sizes at the respective layer, i.e., build height z_{glob}.

The continuous decrease in the G/R ratio for the process velocities of 3 m/min or 4.5 m/min, as shown in Figure 8, is reflected in a decrease in the proportion of columnar morphology, as shown by the green and yellow data points in Figure 10a. For the growth velocity of 1.5 m/min, the constantly high absolute values of the G/R ratios at $z = 0$ (Figure 8a) and at $x \approx 0$ (Figure 8b) result in a higher proportion of columnar morphology over the entire wall height, despite the contrary trends between the G/R ratio at $z = 0$ (Figure 8a) and $x \approx 0$ (Figure 8b).

For all parameter combinations, the grain size decreases from about µm to about 60^{+10}_{-10} µm within the first 5 mm, i.e., the first 10 layers, and remains constant at this level up to a build height of about z_{glob} = 20 mm. Beyond a z_{glob} of > 20 mm, the grain size increases continuously. The circular accumulation of material at the top of the wall in Figure 9a, which results from excessive heat accumulation, coincides with the occurrence of large equiaxed dendritic grains of an average size of 180^{+20}_{-12} µm.

4. Discussion

The results presented in Figures 9 and 10 show a significant influence of the process parameters on the grain structure in DED-manufactured samples, as expected by the hypothesis of this paper. Figure 11 correlates the determined temperature gradients and solidification rates of Figures 6b and 7b with each other in the manner of a typical solidification structure map. The data points of each parameter combination represent the values during the deposition of the layers at the height z_{glob}, where the morphology transits from columnar to equiaxed dendritic grains. This transitional height is identified by the position, where the proportion of the columnar grains in Figure 10a falls below a value of 0.5. The three data points of each parameter combination represent the values during the deposition of the transitional layer as well as the values of five layers before the transitional layer and five layers after the transitional layer. The thin grey curves represent the constant cooling rates, and the dashed grey lines represent the constant G/R ratios.

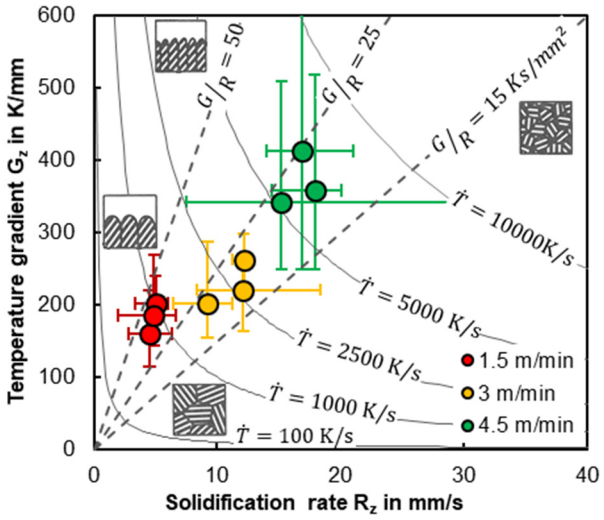

Figure 11. Temperature gradients and solidification rates at the build height, where the morphology transits from columnar to equiaxed dendritic grains. The colour of the data points marks the process parameters, as listed in Table 1.

The representation in the map shows that the G/R ratio at the transitional build height is comparably high at $G/R \approx 25$ Ks/mm^2 for all investigated parameter combinations. The cooling rates are much higher for the case of deposition with a higher process velocity. The different process parameters in L-DED manufacturing led to distinctly different solidification regimes, which can be clearly distinguished from each other in the solidification structure map in Figure 11. This proves the significant influence of the process parameters on solidification in L-DED manufacturing, which potentially enables the development of optimization strategies for appropriate control in local grain structures. However, according to Equation (3), a change in the velocity is associated with the frequency of layer deposition, which affects the heat accumulation shown in Figure 5. The development of process strategies requires knowledge about the individual influence of heat accumulation and process parameters. In order to distinguish the effect of the process parameters from the effect of heat accumulation, the layer frequency, f_{Layer}, is adjusted independently from the process velocity by the DED manufacturing of samples with different perimeters, $l_{contour}$, as shown in Figure 1 and listed in Table 1.

Figure 12 presents the influence of the layer frequency on the heat accumulation effect by the representative value of the residual temperature after 50 layers. The value of the data points represents the average value of the local temperature minima, i.e., residual temperature values, between the 49th and 51st layers in three repeats. The minimum and maximum extension of the error bars represent the minimum and maximum deviations,

which are represented with the grey scatter band in Figure 5, at nine local temperature minima that result from the three minima between the 49th and 51st layers in three repeats.

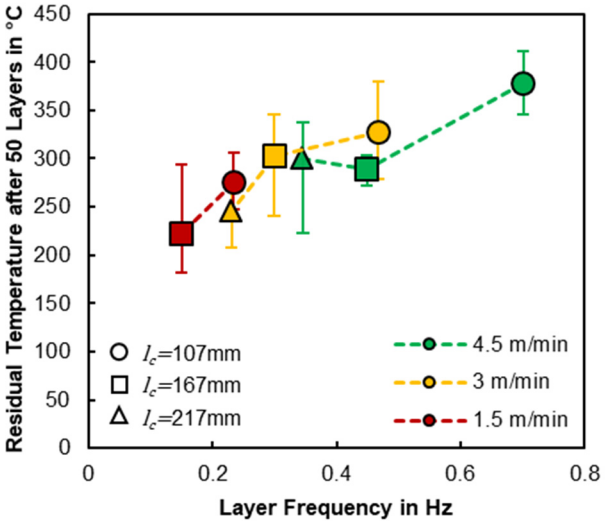

Figure 12. Average residual temperature of the previous layer after deposition of the 50th ± 1 layer in the case of DED manufacturing of samples with different sizes at different process parameter combinations. The shape and the colour of the data points mark the sample perimeter and the process parameters, as listed in Table 1.

Figure 12 shows that the residual temperature increases with the increasing layer frequency but is almost independent of other process parameters, such as laser power and process velocity. The comparison of the yellow triangle with the red circle, the yellow square with the green triangle, or the green square with the yellow triangle indicates that for a given frequency, DED manufacturing using different process parameters leads to comparable residual temperatures after 50 layers. This close correlation between layer frequency and residual temperature demonstrates that the major influence on heat accumulation is the layer frequency.

In order to analyse the influence of the layer frequency and the accompanying heat accumulation on the solidification at the lower part of the melt pool at $x = 0$, the temperature gradients and solidification rates, as well as the resulting G/R ratio and cooling rate after 50^{+1}_{-1} layers are compared in Figure 13. The individual data points represent the average of the values at 50^{+1}_{-1} layer, obtained from the measurements presented in Figures 6–8 for the samples with a perimeter of $l_{contour} \approx 107$ mm and those presented in parts in the Appendix A for $l_{contour} \approx 167$ mm and $l_{contour} \approx 217$ mm. The length of the error bars represents the range between the minimum and the maximum scatter between the 49th and 51st layers.

Figure 13a shows that the temperature gradient in the z-direction at $x = 0$ is directly influenced by both the heat accumulation and the process parameter combination. On the one hand, for a given process parameter combination, a higher layer frequency leads to a lower temperature gradient after 50 layers. On the other hand, for a given layer frequency, the parameter combination with a higher process velocity gives rise to a higher temperature gradient after 50 layers.

No correlation can be identified between the layer frequency and the solidification rate after 50 layers in the lower region of the melt pool at (z_{max}-0.5) < z < z_{max} (Figure 13b). Substantial changes in the solidification rate are mainly associated with the process velocity. This reflects the proportional influence of the process velocity on the solidification rate stated in Equation (1) and demonstrates the insignificant influence of heat accumulation on the local solidification rate, as identified in Figure 7b.

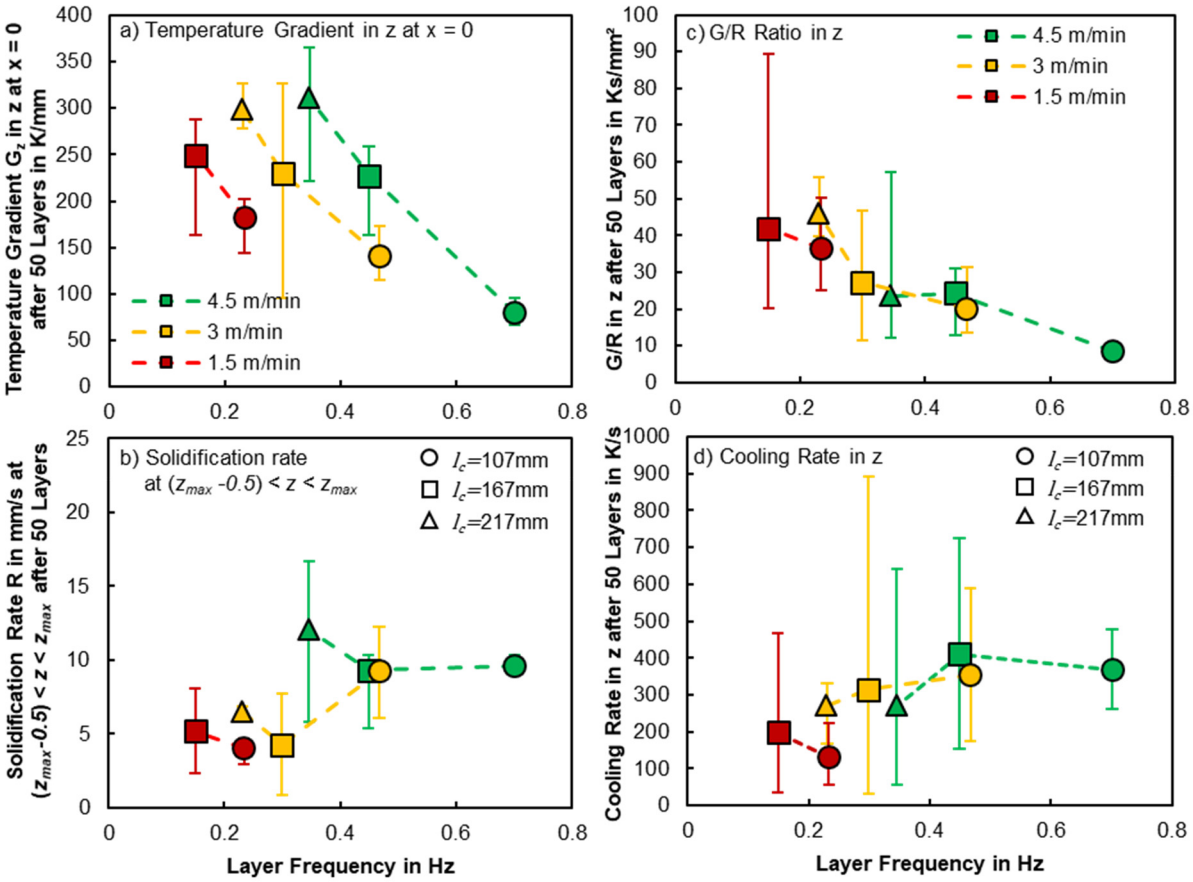

Figure 13. Temperature gradient G_z (**a**) and solidification rate R (**b**), G/R ratio (**c**), and cooling rate (**d**) in z-direction at $x = 0$ after deposition of the 50th $\pm$ 1 layer. The shape and the colour of the data points mark the sample perimeter and the process parameter.

The resulting G/R ratio after 50 layers, in Figure 13c, indicates a correlation to layer frequency, which is characterised by a slight decrease in the G/R ratio with an increasing layer frequency. However, this does not exclude the strong influence of the process velocity, which significantly affects the G/R ratio via the solidification rate.

In the case of the cooling rate in Figure 13d, the influence of the process velocity via the solidification rate is more pronounced than the influence of the layer frequency via heat accumulation.

From Figure 13, one can conclude that the temperature gradient and the G/R ratio, after adding a significant number of superimposed layers, are strongly influenced by heat accumulation, while the solidification and the cooling rate mainly depend on process velocity during DED manufacturing. In order to obtain a high cooling rate and low G/R ratio, it is beneficial to deposit with a maximum process velocity. In order to achieve homogeneous solidification conditions over a large build height z_{glob}, a minimum layer frequency is advantageous. The comparison of the resulting grain structures and the findings above leads to the recommendation that, in order to obtain a refined equiaxed grain structure with enhanced mechanical properties, it is beneficial to reduce the layer frequency and increase the process velocity.

5. Conclusions

The temporally and spatially resolved measurements enabled a comprehensive experimental investigation of the relationship between the process parameters, heat accumulation, solidification conditions, and local grain structure in L-DED.

The analysis of the infrared videos shows that the layer-wise heat input accumulates and leads to an increase in the residual temperature between the subsequent depositions of the individual layers. Depending on the process parameter, it leads to a temperature increase of up to 400 K after the deposition of 50 layers. This heat accumulation coincides with a significant decrease in the temperature gradient of up to 100 K/mm at the solidification zone of the current layer, while the local solidification rate is insignificantly affected.

The comprehensive comparison of the different process parameters for the first time experimentally identifies the key parameters responsible for heat accumulation phenomena and their resulting effect on solidification. This is especially relevant for the increase in the frequency of layer application results in an enhanced heat accumulation, i.e., in a higher magnitude of the increase in residual temperature, which coincides with a stronger decrease in the temperature gradient of solidification. The microstructural analysis shows that the enhanced heat accumulation at high layer frequencies favours a change in the microstructure within low build heights, while low layer frequencies lead to a homogeneous morphology and grain size over a large range of build heights.

Additionally, the new findings suggest strategies for adjusting the identified key parameters to reduce heat accumulation and avoid changes in solidification. The determined optimization strategy reveals that an equiaxed dendritic grain structure over a large range of the built part can be achieved by manufacturing parts at high process velocities and low layer frequencies in L-DED. Finally, the study presents the comprehensive quantitative values of the solidification variables at different locations and times, which contribute to the calibration of numerical models and the development of specific materials for L-DED manufacturing.

Supplementary Materials: The following supporting information can be downloaded at: https://www.mdpi.com/article/10.3390/met12101601/s1, the supplementary data of this work contains three exemplary infrared videos, and the raw data of all recorded temperature fields are available at [39].

Author Contributions: Conceptualization, C.H., P.O., A.M. and W.X.; methodology, C.H. and P.O.; software, C.H. and P.O.; investigation, C.H.; writing—original draft preparation, C.H. and P.O.; writing—review and editing, W.X., A.M., M.E. and M.B.; visualization, C.H.; supervision, W.X., A.M., M.E. and M.B. All authors have read and agreed to the published version of the manuscript.

Funding: The work of Christian Hagenlocher was funded by the Alexander von Humboldt Foundation within the framework of a Feodor-Lynen-Scholarship.

Data Availability Statement: The raw/processed data required to reproduce these findings can be downloaded at https://doi.org/10.18419/darus-2242 [39].

Conflicts of Interest: The authors declare no conflict of interest. The funders had no role in the design of the study; in the collection, analyses, or interpretation of data; in the writing of the manuscript; or in the decision to publish the results.

Appendix A

The appendix presents the temperature measurements with their resulting temperature gradients and cooling rates of the larger perimeters, $l_{contour} \approx 167$ mm and $l_{contour} \approx 217$ mm, listed in Table 1.

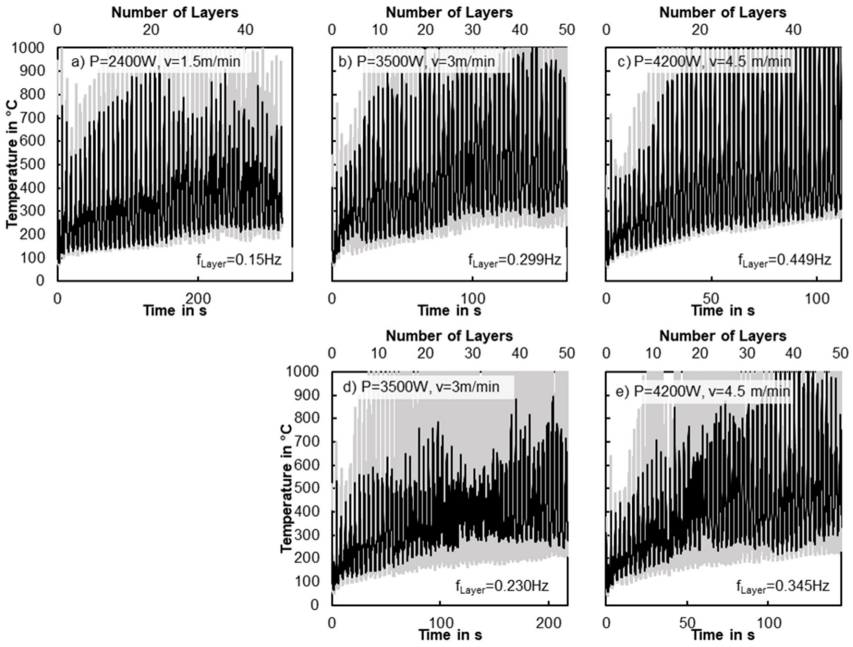

Figure A1. Average temperature at $z = 0^{+0.5}_{-0}$ and $x_{glob} = 0 \pm v_{proc} \cdot t_{shut}$ as a function of time during L-DED manufacturing of rectangular parts with a perimeter of $l_{contour} \approx 167$ mm (**a**–**c**) and $l_{contour} \approx 217$ mm (**d**,**e**) at a laser power of 2.4 kW and a process velocity of 1.5 m/min (**a**), 3.5 kW and 3 m/min (**b**,**d**), and 4.2 kW and 4.5 m/min (**c**,**e**). The grey scatter band represents the minimum and maximum deviations of all pixels within $z = 0^{+0.5}_{-0}$ and $x_{glob} = 0 \pm v_{proc} \cdot t_{shut}$ within three repetitive measurements.

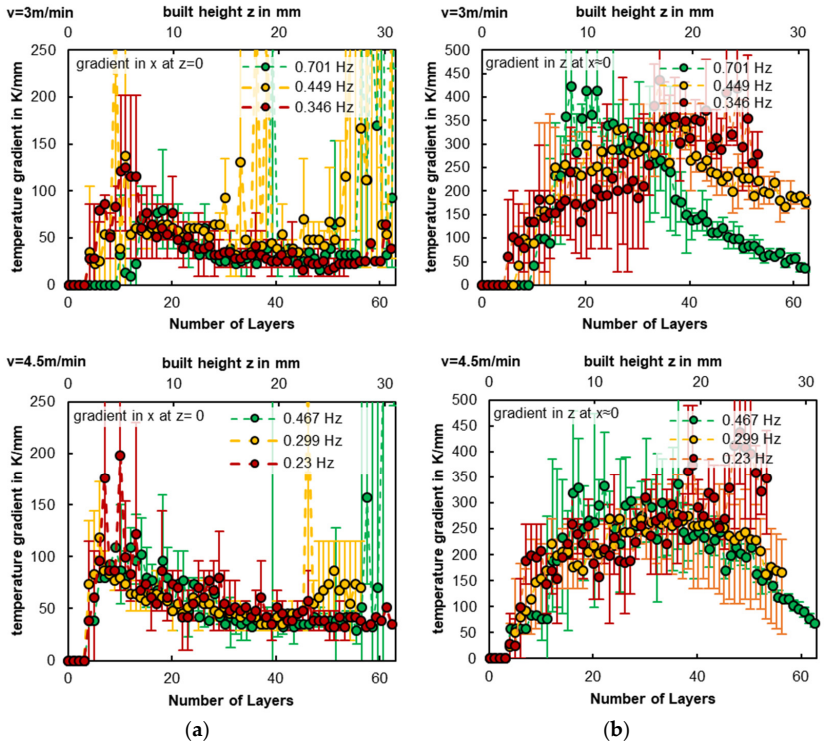

Figure A2. Comparison of gradient evolution in the case of constant process velocities and different frequencies. Average temperature gradients during solidification at $z = 0$ (**a**) and $x = 0$ (**b**) as a function of the number of added layers and build height in the case of DED manufacturing of parts with a perimeter of $l_{contour} \approx 167$ mm and $l_{contour} \approx 217$ mm for different process parameter combinations.

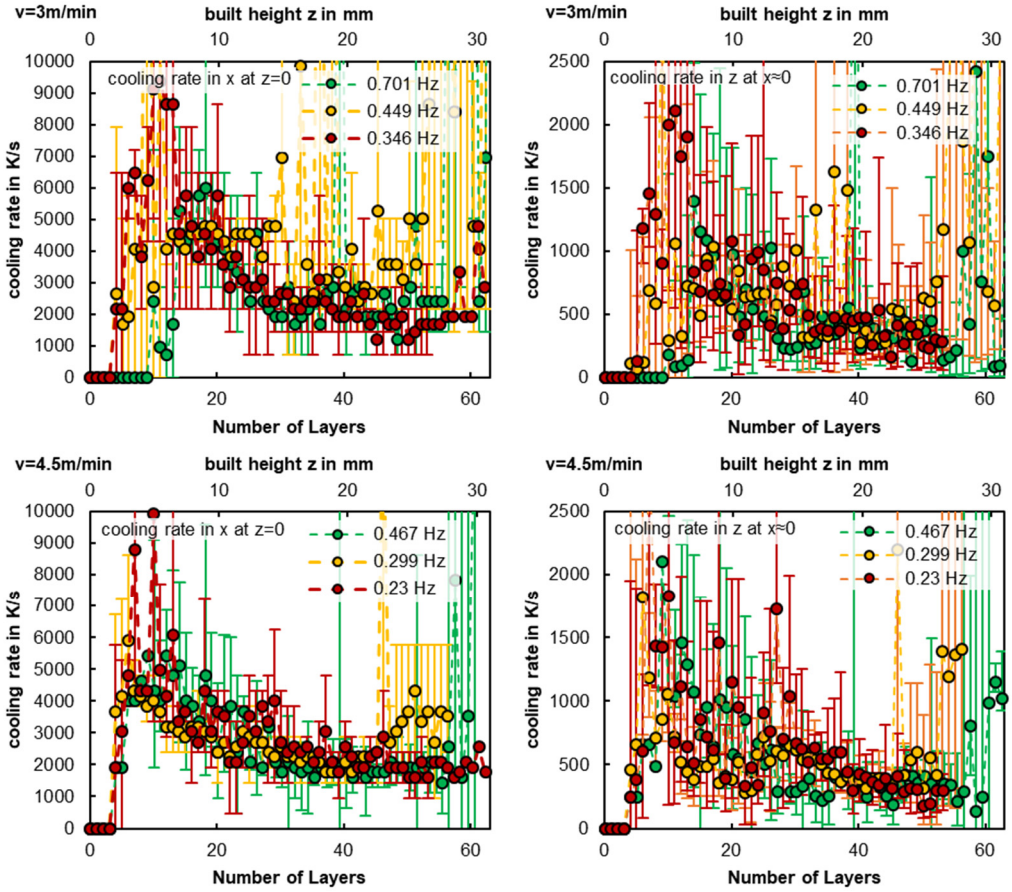

Figure A3. Average cooling rates during solidification at $z = 0$ (**a**) and $x = 0$ (**b**) as a function of the number of added layers and build height in the case of DED manufacturing of parts with a perimeter of $l_{contour} \approx 167$ mm and $l_{contour} \approx 217$ mm for different process parameter combinations.

References

1. Fujita, H.; Tabata, T. The effect of grain size and deformation sub-structure on mechanical properties of polycrystalline aluminum. *Acta Metall.* **1973**, *21*, 355–365. [CrossRef]
2. Wyrzykowski, J.W.; Grabski, M.W. The Hall-Petch relation in aluminium and its dependence on the grain boundary structure. *Philos. Mag. A* **1986**, *53*, 505–520. [CrossRef]
3. Kempf, A.; Hilgenberg, K. Influence of sub-cell structure on the mechanical properties of AlSi10Mg manufactured by laser powder bed fusion. *Mater. Sci. Eng. A* **2020**, *776*, 138976. [CrossRef]
4. Froend, M.; Ventzke, V.; Dorn, F.; Kashaev, N.; Klusemann, B.; Enz, J. Microstructure by design: An approach of grain refinement and isotropy improvement in multi-layer wire-based laser metal deposition. *Mater. Sci. Eng. A* **2020**, *772*, 138635. [CrossRef]
5. Froend, M.; Ventzke, V.; Riekehr, S.; Kashaev, N.; Klusemann, B.; Enz, J. Microstructure and microhardness of wire-based laser metal deposited AA5087 using an Ytterbium fibre laser. *Mater. Charact.* **2018**, *143*, 59–67. [CrossRef]
6. Chen, R.; Wang, H.; He, B.; Tu, Y.; Tang, H. Effect of thermal cycling on microstructure and mechanical properties of 2A97 Al-Li alloy fabricated by direct laser deposition. *Vacuum* **2021**, *190*, 110299. [CrossRef]
7. Thompson, S.M.; Bian, L.; Shamsaei, N.; Yadollahi, A. An overview of Direct Laser Deposition for additive manufacturing; Part I: Transport phenomena, modeling and diagnostics. *Addit. Manuf.* **2015**, *8*, 36–62. [CrossRef]
8. Zhao, X.; Lv, Y.; Dong, S.; Yan, S.; He, P.; Liu, X.; Liu, Y.; Lin, T.; Xu, B. The effect of thermal cycling on direct laser-deposited gradient H13 tool steel: Microstructure evolution, nanoprecipitation behaviour, and mechanical properties. *Mater. Today Commun.* **2020**, *25*, 101390. [CrossRef]
9. Yan, F.; Xiong, W.; Faierson, E.J. Grain structure control of additively manufactured metallic materials. *Materials* **2017**, *10*, 1260. [CrossRef]
10. Shamsaei, N.; Yadollahi, A.; Bian, L.; Thompson, S.M. An overview of Direct Laser Deposition for additive manufacturing; Part II: Mechanical behavior, process parameter optimization and control. *Addit. Manuf.* **2015**, *8*, 12–35. [CrossRef]
11. Foster, B.K.; Am Beese Keist, J.S.; McHale, E.T.; Palmer, T.A. Impact of interlayer dwell time on microstructure and mechanical properties of nickel and titanium alloys. *Metall. Mater. Trans. A* **2017**, *48*, 4411–4422. [CrossRef]

12. Kou, S. *Welding Metallurgy*, 2nd ed.; John Wiley & Sons: Hoboken, NJ, USA, 2003.
13. Hagenlocher, C.; O'Toole, P.; Xu, W.; Brandt, M.; Easton, M.A.; Molotnikov, A. In process monitoring of the thermal profile during solidification in laser directed energy deposition of aluminium. *Addit. Manuf. Lett.* **2022**, *3*, 100084. [CrossRef]
14. Patel, M.N.; Qiu, D.; Wang, G.; Gibson, M.A.; Prasad, A.; StJohn, D.H.; Easton, M.A. Understanding the refinement of grains in laser surface remelted Al-Cu alloys. *Scr. Mater.* **2020**, *178*, 447–451. [CrossRef]
15. Prasad, A.; Yuan, L.; Lee, P.; Patel, M.; Qiu, D.; Easton, M.; StJohn, D. Towards understanding grain nucleation under Additive Manufacturing solidification conditions. *Acta Mater.* **2020**, *195*, 392–403. [CrossRef]
16. Kurz, W.; Fisher, D.J.D. *Fundamentals of Solidification*; Trans Tech Publications: Zurich-Durnten, Switzerland, 1986.
17. Schempp, P.; Rethmeier, M. Understanding grain refinement in aluminium welding. *Weld. World* **2015**, *59*, 767–784. [CrossRef]
18. Zhang, K.; Tian, X.; Bermingham, M.; Rao, J.; Jia, Q.; Zhu, Y.; Wu, X.; Cao, S.; Huang, A. Effects of boron addition on microstructures and mechanical properties of Ti-6Al-4V manufactured by direct laser deposition. *Mater. Des.* **2019**, *184*, 108191. [CrossRef]
19. Zhang, H.; Zhu, H.; Nie, X.; Yin, J.; Hu, Z.; Zeng, X. Effect of Zirconium addition on crack, microstructure and mechanical behavior of selective laser melted Al-Cu-Mg alloy. *Scr. Mater.* **2017**, *134*, 6–10. [CrossRef]
20. Wu, D.; Huang, Y.; Niu, F.; Ma, G.; Yan, S.; Li, C.; Ding, J. Effects of TiO2 doping on microstructure and properties of directed laser deposition alumina/aluminum titanate composites. *Virtual Phys. Prototyp.* **2019**, *14*, 371–381. [CrossRef]
21. Martin, J.H.; Yahata, B.; Mayer, J.; Mone, R.; Stonkevitch, E.; Miller, J.; Mark, R.O.; Schaedler, T.; Hundley, J.; Callahan, P.; et al. Grain refinement mechanisms in additively manufactured nano-functionalized aluminum. *Acta Materialia* **2020**, *200*, 1022–1037. [CrossRef]
22. Bolzoni, L.; Xia, M.; Babu, N.H. Formation of equiaxed crystal structures in directionally solidified Al-Si alloys using Nb-based heterogeneous nuclei. *Sci. Rep.* **2016**, *6*, 39554. [CrossRef]
23. Zhang, D.; Prasad, A.; Bermingham, M.J.; Todaro, C.J.; Benoit, M.J.; Patel, M.N.; Qiu, D.; StJohn, D.H.; Qian, M.; Easton, M.A. Grain refinement of alloys in fusion-based additive manufacturing processes. *Metall. Mater. Trans. A* **2020**, *51*, 4341–4359. [CrossRef]
24. Rykalin, N.N. *Calculations of Thermal Processes in Welding*; Mashgiz: Moscow, Russia, 1960.
25. Cline, H.E.; Anthony, T.R. Heat treating and melting material with a scanning laser or electron beam. *J. Appl. Phys.* **1977**, *48*, 3895. [CrossRef]
26. Hagenlocher, C.; Fetzer, F.; Weller, D.; Weber, R.; Graf, T. Explicit analytical expressions for the influence of welding parameters on the grain structure of laser beam welds in aluminium alloys. *Mater. Des.* **2019**, *174*, 107791. [CrossRef]
27. Hagenlocher, C.; Seibold, M.; Weber, R.; Graf, T. Modulation of the local grain structure in laser beam welds to inhibit the propagation of centerline hot cracks. *Procedia CIRP* **2018**, *74*, 434–437. [CrossRef]
28. Zhou, Y.; Chen, S.; Chen, X.; Liang, J.; Liu, C.; Wang, M. The effect of laser scanning speed on microstructural evolution during direct laser deposition 12CrNi2 alloy steel. *Opt. Laser Technol.* **2020**, *125*, 106041. [CrossRef]
29. Froend, M.; Ventzke, V.; Kashaev, N.; Klusemann, B.; Enz, J. Thermal analysis of wire-based direct energy deposition of Al-Mg using different laser irradiances. *Addit. Manuf.* **2019**, *29*, 100800. [CrossRef]
30. Wang, T.; Zhu, Y.Y.; Zhang, S.Q.; Tang, H.B.; Wang, H.M. Grain morphology evolution behavior of titanium alloy components during laser melting deposition additive manufacturing. *J. Alloy. Compd.* **2015**, *632*, 505–513. [CrossRef]
31. Chiumenti, M.; Lin, X.; Cervera, M.; Lei, W.; Zheng, Y.; Huang, W. Numerical simulation and experimental calibration of additive manufacturing by blown powder technology. Part I: Thermal analysis. *Rapid Prototyp. J.* **2017**, *23*, 448–463. [CrossRef]
32. Denlinger, E.R.; Heigel, J.C.; Michaleris, P.; Palmer, T.A. Effect of inter-layer dwell time on distortion and residual stress in additive manufacturing of titanium and nickel alloys. *J. Mater. Processing Technol.* **2015**, *215*, 123–131. [CrossRef]
33. Haley, J.; Leach, C.; Jordan, B.; Dehoff, R.; Paquit, V. In-situ digital image correlation and thermal monitoring in directed energy deposition additive manufacturing. *Opt. Express* **2021**, *29*, 9927–9941. [CrossRef]
34. Promoppatum, P.; Yao, S.-C.; Pistorius, P.C.; Rollett, A.D.; Coutts, P.J.; Lia, F.; Martukanitz, R. Numerical modeling and experimental validation of thermal history and microstructure for additive manufacturing of an Inconel 718 product. *Prog. Addit. Manuf.* **2018**, *3*, 15–32. [CrossRef]
35. Becker, D.; Boley, S.; Eisseler, R.; Stehle, T.; Möhring, H.-C.; Onuseit, V.; Hoßfeld, M.; Graf, T. Influence of a closed-loop controlled laser metal wire deposition process of S Al 5356 on the quality of manufactured parts before and after subsequent machining. *Prod. Eng.* **2021**, *15*, 489–507. [CrossRef]
36. Zhang, K.; Yu, K.; Liu, Y.; Zhao, Y. Effect of surface oxidation on emissivity properties of pure aluminum in the near infrared region. *Mater. Res. Express* **2017**, *4*, 86501. [CrossRef]
37. Wen, C.-D.; Mudawar, I. Emissivity characteristics of roughened aluminum alloy surfaces and assessment of multispectral radiation thermometry (MRT) emissivity models. *Int. J. Heat Mass Transf.* **2004**, *47*, 3591–3605. [CrossRef]
38. Touloukian, Y.S.; DeWitt, D.P. Thermophysical properties of matter-the tprc data series. In *Thermal Radiative Properties-Metallic Elements and Alloys*; Purdue University: West Lafayette, IN, USA, 1970; Volume 7.
39. Hagenlocher, C.; Boley, S. Infrared Imaging of Laser Based Direct Energy Deposition of AlMg5 Wire. 2021. Available online: https://doi.org/10.18419/darus-2242 (accessed on 1 April 2021).

40. Barker, L.J. Revealing the grain structure of common aluminum alloy metallographic specimens. *Trans. ASM* **1950**, *42*, 347.
41. Stahl-Mikrophotographische Bestimmung der Erkennbaren Korngröße(DIN EN ISO 643: 2019, Korrigierte Fassung 2020-03): Steels—Micrographic Determination of the Apparent Grain Size (ISO 643:2019, Corrected Version 2020-03), Beuth Verlag GmbH, 2017. Available online: https://www.beuth.de/de/norm-entwurf/din-en-iso-643/276478455 (accessed on 1 April 2021).